

We are IntechOpen, the world's leading publisher of Open Access books Built by scientists, for scientists

6,900

Open access books available

186,000

International authors and editors

200M

Downloads

Our authors are among the

154

Countries delivered to

TOP 1%

most cited scientists

12.2%

Contributors from top 500 universities



WEB OF SCIENCE™

Selection of our books indexed in the Book Citation Index
in Web of Science™ Core Collection (BKCI)

Interested in publishing with us?
Contact book.department@intechopen.com

Numbers displayed above are based on latest data collected.
For more information visit www.intechopen.com



New Observations by Wind Profiling Radars

Masayuki K. Yamamoto

*Research Institute for Sustainable Humanosphere (RISH), Kyoto University,
Japan*

1. Introduction

Wind profiling radar, also referred to as “radar wind profiler”, “wind profiler”, and “clear-air Doppler radar”, is used to measure height profiles of vertical and horizontal winds in the troposphere. It receives signals scattered by radio refractive index irregularities (clear-air echo) and measures the Doppler shift of the scattered signals (Gage, 1990). Wind profiling radar measures wind velocities by steering its beam directions or using spaced receiving antennas (e.g., Larsen & Röttger 1989; May, 1990). The two methods are referred to as the Doppler beam swinging (DBS) technique and spaced antenna (SA) technique, respectively. Owing to its capability to measure wind velocities in the clear air with high height and time resolutions (typically a hundred to several hundreds of meters and less than several minutes, respectively), it is used for atmospheric research such as radio wave scattering, gravity waves, turbulence, temperature and humidity profiling, precipitation system, and stratosphere-troposphere exchange (STE) processes (Fukao, 2007; Hocking, 2011). Wind profiling radar is also utilized for monitoring wind variations routinely. In USA and Japan, a nationwide ultrahigh frequency (UHF) wind-profiling radar network is operated in order to provide upper-air wind data to numerical weather prediction (Ishihara et al., 2006; Stanley et al., 2004). In Europe, Cost Wind Initiative for a Network Demonstration in Europe (CWINDE), now renamed as the Co-Ordinated Wind Profiler Network in Europe, is also operated (Met Office, 2011).

For wind profiling radars, frequency range of 30-3000 MHz (i.e., very high frequency (VHF) and UHF bands) is generally used because the energy spectrum of atmospheric turbulence falls off rapidly with decreasing eddy size in the inertia subrange, and radar radio waves are scattered only from turbulent eddies at the Bragg scale (i.e., half the radar wavelength). For measurements from the ground to several thousand meters, UHF wind profiling radars are widely used because their small antenna size enables their easy installation and their quick switching time from transmission to reception is necessary for measurements near the ground. Such UHF wind profiling radars are referred to as the boundary layer radars. Because the minimum size of turbulent eddies increases exponentially with increasing altitude (e.g., Hocking, 1985), frequencies near 50 MHz are used for clear-air radars which measure the mesosphere, stratosphere and troposphere (MST radars) and those which measure the stratosphere and troposphere (ST radars). In the chapter, measurement results of VHF and UHF radars are presented.

Recent development in radar interferometry techniques provides means for enhancing radar resolution and improving data quality. In radar interferometry, spaced receiver antennas are used to improve angular resolution, and multiple carrier frequencies are used to improve range resolution. The former is referred to as coherent radar imaging (CRI) or spatial domain interferometric imaging (SDI; Palmer et al., 1998; Hassenpflug et al., 2008), and the latter is referred to as range imaging (RIM; Palmer et al., 1999) or frequency-domain interferometric imaging (FII; Luce et al., 2001). Hereafter the abbreviations CRI and RIM are used. Though development of the radar interferometry technique have decades of history (Hocking, 2011), CRI and RIM, which have been intensively developed for the last decade, are presented in section 2.

Wind profiling radars operated at approximately 50 MHz frequency (50-MHz wind profiling radars) are not sensitive for small-sized cloud particles. Therefore 50-MHz wind profiling radars are able to measure vertical and horizontal wind velocities in both the clear air and cloudy regions. Millimeter-wave radars, which use near 35-GHz or 95-GHz frequency (i.e., 8-mm or 3-mm wavelength) and hence are able to detect echoes scattered by small-sized cloud particles, are an indispensable means to measure microphysical properties of clouds (Kollias et al., 2007). Laser radars (lidars), which transmit laser light and receive echoes scattered by atmospheric molecules, aerosols, and hydrometeors, are useful to measure not only various physical quantities in the clear air but also particles and hydrometeors in the atmosphere (Wandinger, 2005). Recent measurements using collocated wind profiling radars and millimeter-wave radars/lidars have gained new insights of turbulence and cloud processes. The measurement results are presented in section 3.

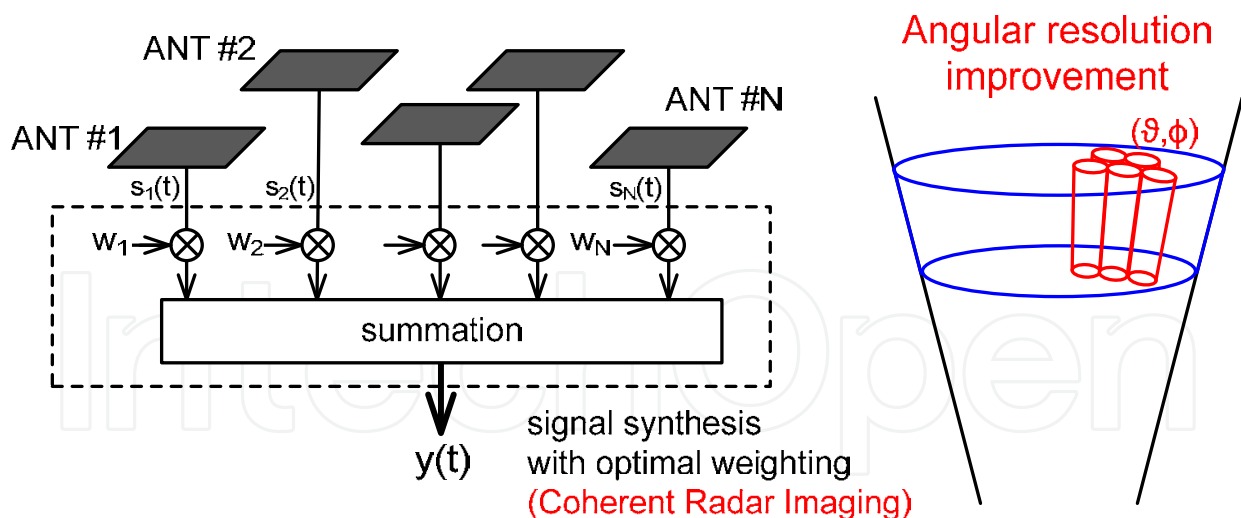


Fig. 1. Conceptual drawing of CRI. The blue-colored volume on the right shows the resolution without CRI (i.e., the angular resolution is determined by the antenna beam width), and the red-colored volumes show the angular resolution improvement attained by CRI.

2. Imaging techniques to enhance radar resolutions

Though development of the radar interferometry techniques have decades of history, CRI and RIM, which have been intensively developed for the last decade, are presented

in section 2.1 and 2.2, respectively. The readers are recommended to refer Hocking (2011) for the thorough development history of the radar interferometry techniques. Further applications aiming at advanced probing of the atmosphere are presented in section 2.3.

2.1 Angular resolution enhancement using spaced receivers

2.1.1 Signal processing

Fig. 1. shows a conceptual drawing of CRI. In CRI, signals from the spaced receivers are synthesized with appropriate weights in order to steer the radar beam in certain directions with improved angular resolution. For CRI, the Capon method (Capon, 1969) is widely used because it satisfies both high angular resolution and simple calculation. Hereafter signal processing of CRI using the Capon method is described. The Capon method is described as the problem of finding optimal weights. The optimal weights used in order to calculate the weighted sum of signals which are received by the spaced receivers. \mathbf{s} denotes a set of signals associated with the N spaced receivers at an arbitrary range gate and expressed by

$$\mathbf{s}(t) = (s_1(t), s_2(t), \dots, s_N(t))^T, \quad (1)$$

where t is the sampled time and T is the transpose operator. \mathbf{w} denotes a set of weights for summation and is expressed by

$$\mathbf{w} = (w_1, w_2, \dots, w_N)^T. \quad (2)$$

The optimal weight vector is given by a solution that minimizes the resulting average power B . B is expressed by

$$B = \mathbf{w}^H \mathbf{R} \mathbf{w}, \quad (3)$$

where H represents the Hermitian operator (conjugate transpose) and \mathbf{R} is a covariance matrix given by

$$\mathbf{R} = \begin{pmatrix} R_{11} & R_{12} & \dots & R_{1N} \\ R_{21} & R_{22} & \dots & R_{2N} \\ \vdots & \vdots & \dots & \vdots \\ R_{N1} & R_{N2} & \dots & R_{NN} \end{pmatrix}, \quad (4)$$

R_{ij} is a covariance between s_i and s_j . The length of time used for calculating \mathbf{R} should be determined by considering the accuracy of covariance value and the time resolution. \mathbf{w} is constrained by the condition of constant gain to waves coming from the target volume, and the constraint is given by

$$\mathbf{e}^H \mathbf{w} = 1, \quad (5)$$

where

$$\mathbf{e} = (e^{jk \cdot D_1}, e^{jk \cdot D_2}, \dots, e^{jk \cdot D_N})^T, \quad (6)$$

\mathbf{k} represents the wavenumber vector of the focused direction with the zenith and azimuth angle of θ and ϕ , respectively ($\mathbf{k} = \frac{2\pi}{\lambda}[\sin\theta\sin\phi, \sin\theta\cos\phi, \cos\theta]$), and the vectors which represent the center of each receiving receiver are denoted by \mathbf{D}_m for the m th receiver. \mathbf{e} is referred to as the steering vector. The constrained minimization problem can be solved using the Lagrange method, and Palmer et al. (1998) describe details of solving the constrained minimization problem (see their appendix). As the solution of the constrained minimization problem, the optimal weight $\mathbf{w}_C(\mathbf{k})$ is given by

$$\mathbf{w}_C(\mathbf{k}) = \frac{\mathbf{R}^{-1}\mathbf{e}}{\mathbf{e}^H\mathbf{R}^{-1}\mathbf{e}}. \quad (7)$$

Using Equations (1) and (7), scalar output of the filter $y(t)$ is given by

$$y(t) = \mathbf{w}_C^H(\mathbf{k})\mathbf{s}(t). \quad (8)$$

By calculating the Doppler spectrum of $y(t)$, brightness B_C (i.e., power density), radial Doppler velocity, and spectral width are able to be computed with improved angular resolution. B_C is able to be obtained without calculating \mathbf{w}_C and given by

$$B_C(\mathbf{k}) = \frac{1}{\mathbf{e}^H\mathbf{R}^{-1}\mathbf{e}}. \quad (9)$$

When the brightness at arbitrary Doppler velocity needs to be calculated, \mathbf{R} is replaced by the cross-spectral matrix of the N receiver signals. Palmer et al. (1998) showed a clear difference in angular distribution of brightness between positive and negative Doppler velocities (see their Plate 2). Brightness at the arbitrary Doppler velocity of received data is also able to be calculated by applying band-pass filtering to \mathbf{s} .

In the Fourier-based method, in which all the signals from receivers were synthesized with equal weight, a weight vector $\mathbf{w}_F(\mathbf{k})$ which steers the beam in the direction \mathbf{k} is given by

$$\mathbf{w}_F(\mathbf{k}) = (e^{j\mathbf{k}\cdot\mathbf{D}_1}, e^{j\mathbf{k}\cdot\mathbf{D}_2}, \dots, e^{j\mathbf{k}\cdot\mathbf{D}_N})^T. \quad (10)$$

Scalar output of the filter is calculated by replacing $\mathbf{w}_C(\mathbf{k})$ in Equation (8) with $\mathbf{w}_F(\mathbf{k})$.

Other methods are able to be used for CRI. Details of multiple signal classification (MUSIC) method and maximum entropy method (MEM) are explained by H elal et al. (2001) and Yu et al. (2000), respectively. For more general review of CRI, see Woodman (1997).

There are factors that affect the performance of CRI. Using numerical simulation, effects of receiver noise and turbulence distribution were evaluated by Yu et al. (2000) and Cheong et al. (2004). Further, Yu et al. (2000) evaluated relation between CRI performance and receiver arrangement. Effects of uncertainty of receiver gain and phase were evaluated for the case of turbulent Eddy Profiler (TEP), which was developed by the University of Massachusetts in order to carry out CRI measurement in the boundary layer (Mead et al. 1998).

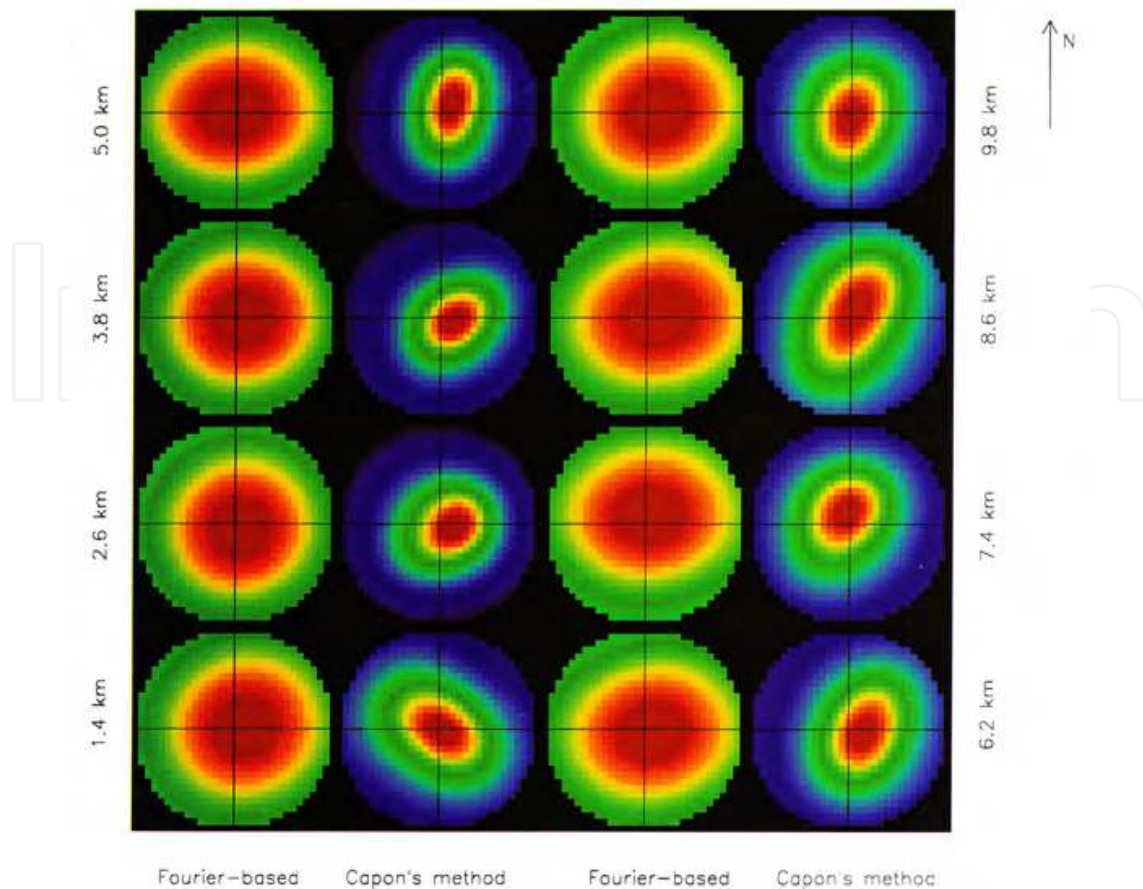


Fig. 2. Brightness distributions within $\pm 4^\circ$ from the center of beam direction at the altitudes from 1.4 km to 9.8 km (Palmer et al., 1998). Red color corresponds to highest brightness. Images on the left and right of each pair were obtained with the Fourier-based method and the Capon method, respectively.

2.1.2 Measurement results

An example of high-angle-resolution measurement using CRI is presented. Fig. 2 shows brightness distributions within $\pm 4^\circ$ from the center of beam direction measured by the Middle and Upper Atmosphere radar (MU radar). MU radar is a MST radar installed at Shigaraki MU Observatory, Japan (34.85°N , 136.10°E ; Fukao et al., 1990). CRI successfully produces fine-scale angular distributions of backscattered clear-air echo power within the two-way half-power full beam width of 2.5° . Such high angular resolution cannot be attained without CRI. It is noted that the Capon method exhibits better resolution than the Fourier-based method. Using data collected by a VHF radar installed at Tourris, France (43.08°N , 6.01°E), H elal et al. (2001) showed a fine-scale angular distribution of backscattered clear-air echo power using the Capon and MUSIC methods. Chau and Woodman (2001) also showed the angular distribution using the Fourier-based method, Capon method, MEM, and the fitting technique. Using the characteristic that raindrop fall velocity is much greater than vertical wind velocity, Palmer et al (2005) demonstrated that fine-scale angular distributions of backscattered power from clear air and that from raindrops are able to be obtained separately. From a CRI measurement by TEP, Pollard et al. (2000) demonstrated that horizontal distribution of refractive index structure function is able to be measured.

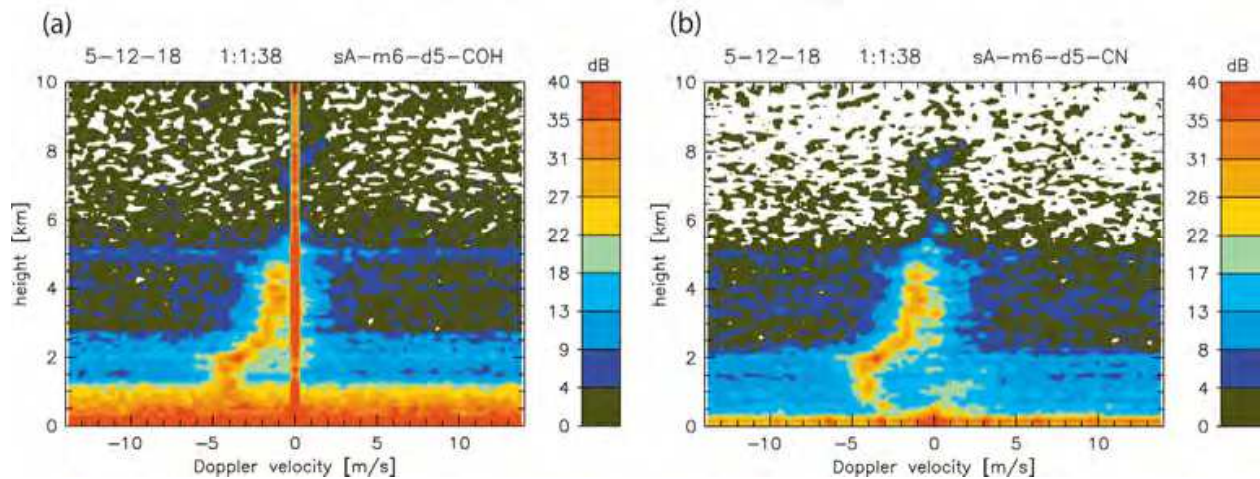


Fig. 3. Altitude profile of Doppler spectra (a) before and (b) after applying clutter mitigation algorithm (Nishimura et al., 2010). Colors show the backscattered power in an arbitrary unit.

CRI is also able to be used for clutter mitigation. Fig. 3 is an example of clutter mitigation. Measurement data were collected by the receiving antenna array of the Equatorial Atmosphere Radar (EAR), which were temporally installed for multistatic radar observations. The EAR is installed at West Sumatra, Indonesia and is operated with a center frequency of 47-MHz and peak output power of 100 kW (Fukao et al., 2003). Strong returns centered at 0 m s⁻¹ in Fig. 3a are signals returned from the ground (i.e., ground clutter), and have to be removed in order to estimate spectral moments correctly. By applying the clutter mitigation algorithm developed by Nishimura et al (2010), the clutter signals are successfully removed (Fig. 3b). Nishimura et al. (2010) attained the clutter mitigation by combining the directional-constrained minimization of power with constrained norm (DCMP-CN; see Kamio et al. (2004) for details) and an algorithm that compensates electromagnetic coupling between antennas and the ground. The compensation was carried out because the electromagnetic coupling can cause a phase error of atmospheric echoes received by antenna arrays, and the phase error can lead to degradation of desired atmospheric echoes in the output of the adaptive clutter mitigation process.

In the case shown by Nishimura et al. (2010), each antenna element has an identical antenna gain. When a high-gain antenna is used for transmission and reception of scattering from atmospheric targets, using auxiliary antennas which are used only for receiving ground clutters is effective for clutter mitigation. In order to realize clutter mitigation using the main antenna of the MU radar and auxiliary antennas, Kamio et al. (2004) modified the DCMP-CN method. In the modified method, the weight of main antenna is kept to 1 in order to keep the main lobe pattern, and the weights of auxiliary antennas are optimized in order to minimize the received power from side lobes.

Moving biological targets like birds and insects can cause a large error of wind velocity measured by wind profiling radars (e.g., Vaughn, 1985; Wilczak et al., 1995). Using CRI, moving clutter is able to be suppressed. From the CRI measurement using TEP, Cheong et al. (2006) succeeded in separating clear-air echoes and the biological scattering which was moving in the grating-lobe region, and demonstrated that the separation of biological scattering greatly reduced the error of wind velocity estimates. Chen et al. (2007) also applied CRI to data measured by multiple antenna profiler radar (MAPR) of National

Center for Atmospheric Research (NCAR) in order to mitigate effects of bird contamination in wind velocity estimates.

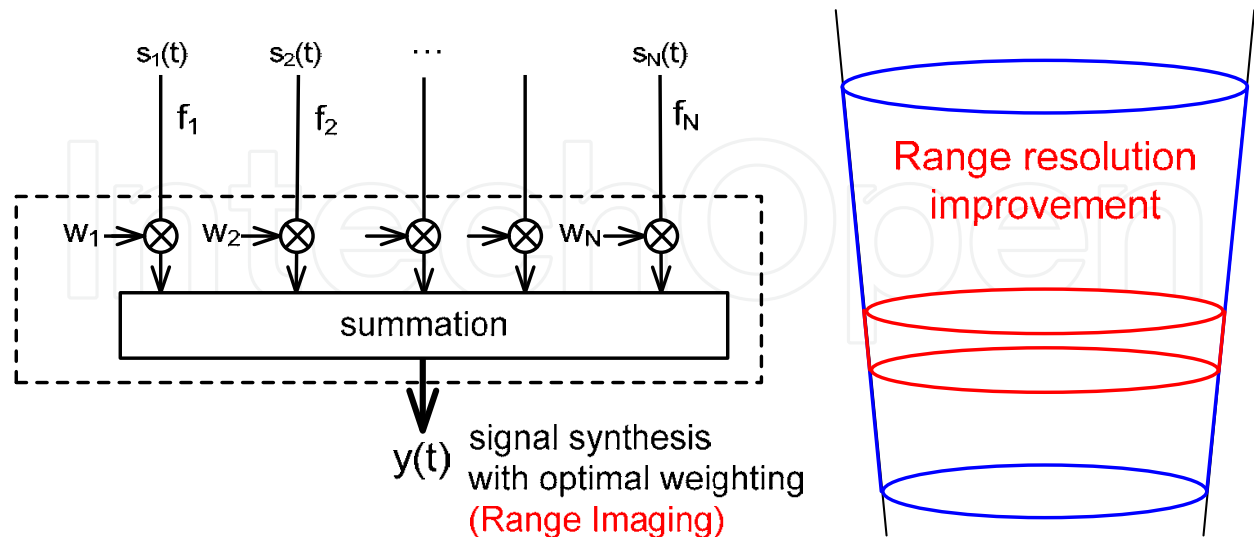


Fig. 4. Conceptual drawing of RIM. The blue-colored volume shows the resolution without RIM (i.e., range resolution is determined by the transmitted pulse width), and the red-colored volume shows the range resolution improvement attained by RIM.

2.2 Range resolution enhancement using multiple frequencies

2.2.1 Signal processing

Figure 4 shows a conceptual drawing of RIM. The width of range gate is determined by the sampling interval of analog-to-digital converter, and the range resolution without RIM is determined by the transmitted pulse width. In RIM, signals sampled from multiple frequencies are synthesized with appropriate weights in the subranges within a range gate. Using the synthesized signal, the first three spectral moments (brightness, Doppler velocity, and spectral width) at the subranges are estimated in order to attain range resolution improvement. Among various methods which can be used for RIM processing (Luce et al., 2001; Palmer, et al., 1998; Smaïni et al., 2002), the Capon method (Capon, 1969) is widely used because it satisfies both high range resolution and simple calculation. Hereafter signal processing of RIM using the Capon method is described. \mathbf{s} denotes a set of signals collected by N carrier frequencies at an arbitrary range gate and is expressed by

$$\mathbf{s}(t) = (s_1(t), s_2(t), \dots, s_N(t))^T. \tag{11}$$

Frequencies are switched on a pulse-to-pulse basis in order to maximize the correlation of signals sampled by different frequencies. Using numerical simulation, Palmer et al. (1999) showed that using 3 or more frequencies are required for RIM measurements. For field measurements, four or five frequencies are used typically (e.g., Fukao et al., 2011; Palmer et al., 2001; Yu & Brown, 2004). The optimal weight vector is given as a solution that minimizes the resulting average power B_r . B_r is expressed by

$$B_r = \mathbf{w}^H \mathbf{R} \mathbf{w}, \tag{12}$$

where \mathbf{w} denotes a set of weights for summation as expressed by Equation (2) and \mathbf{R} is a covariance matrix as expressed by Equation (4). \mathbf{w} is constrained by the condition of constant gain to waves coming from the target range, and the constraint is given by

$$\mathbf{e}^H \mathbf{w} = 1, \quad (13)$$

where \mathbf{e} is a range steering vector and given by

$$\mathbf{e} = (e^{-j(2k_1 r_1 - \phi_1)}, e^{-j(2k_2 r_1 - \phi_2)}, \dots, e^{-j(2k_N r_1 - \phi_N)})^T, \quad (14)$$

where k_m denotes the wavenumber of m th frequency, r_1 represents the range between the target and radar, and ϕ_m is the initial phase of m th frequency.

Because ϕ_m is determined not only by the total system delay throughout the transmitter and receiver chains but also by k_m , the values of ϕ_1, \dots, ϕ_N are different. Therefore the total system delay, from which the values of ϕ_1, \dots, ϕ_N are computed, needs to be known in order to determine \mathbf{e} correctly. Chilson et al. (2004) and Palmer et al. (2001) measured the total system delay by leaking the transmitted signal back to the receiver through an ultrasonic delay line. In a practical manner, only the relative phase differences among the frequencies are necessary to correct the effects of system delay. Therefore, the correction is able to be attained by calculating the phase term of cross correlation between the two time series of received signals measured at different frequencies (Chen, 2004). Measurement results of phase correction using the clear-air echoes are shown by Chen et al. (2009, 2010) and Chen & Zecha (2009).

The optimal weight \mathbf{w}_{rC} is given by

$$\mathbf{w}_{\text{rC}} = \frac{\mathbf{R}^{-1} \mathbf{e}}{\mathbf{e}^H \mathbf{R}^{-1} \mathbf{e}}. \quad (15)$$

Using Equations (11) and (15), scalar output of the filter $y(t)$ is given by

$$y(t) = \mathbf{w}_{\text{rC}}^H \mathbf{s}(t). \quad (16)$$

By calculating Doppler spectrum of $y(t)$, brightness B_{rC} (i.e., power density) and other spectral parameters are able to be computed with improved range resolution. B_{rC} is given by

$$B_{\text{rC}} = \frac{1}{\mathbf{e}^H \mathbf{R}^{-1} \mathbf{e}}. \quad (17)$$

Brightness at arbitrary Doppler velocity is also able to be calculated in the same manner as described in section 2.1.1.

Because of the limited width of transmitted pulse (i.e., wave form of transmitted pulse), received signal power within the range gate has range dependency (i.e., the received signal power decreases near the edge of range gate). Chen and Zecha (2009) proposed a practical method in order to correct the range weighting, and the correction results are also presented by Chen et al. (2009, 2010) and Chen & Zecha (2009).

Recently, Le et al. (2010) proposed a technique that improves received signal power by exploiting the temporal correlation difference between the desired signal and system noise. Le et al. (2010) showed that the technique has better performance of radar echo production than RIM in the low SNR regions.

2.2.2 Measurement results

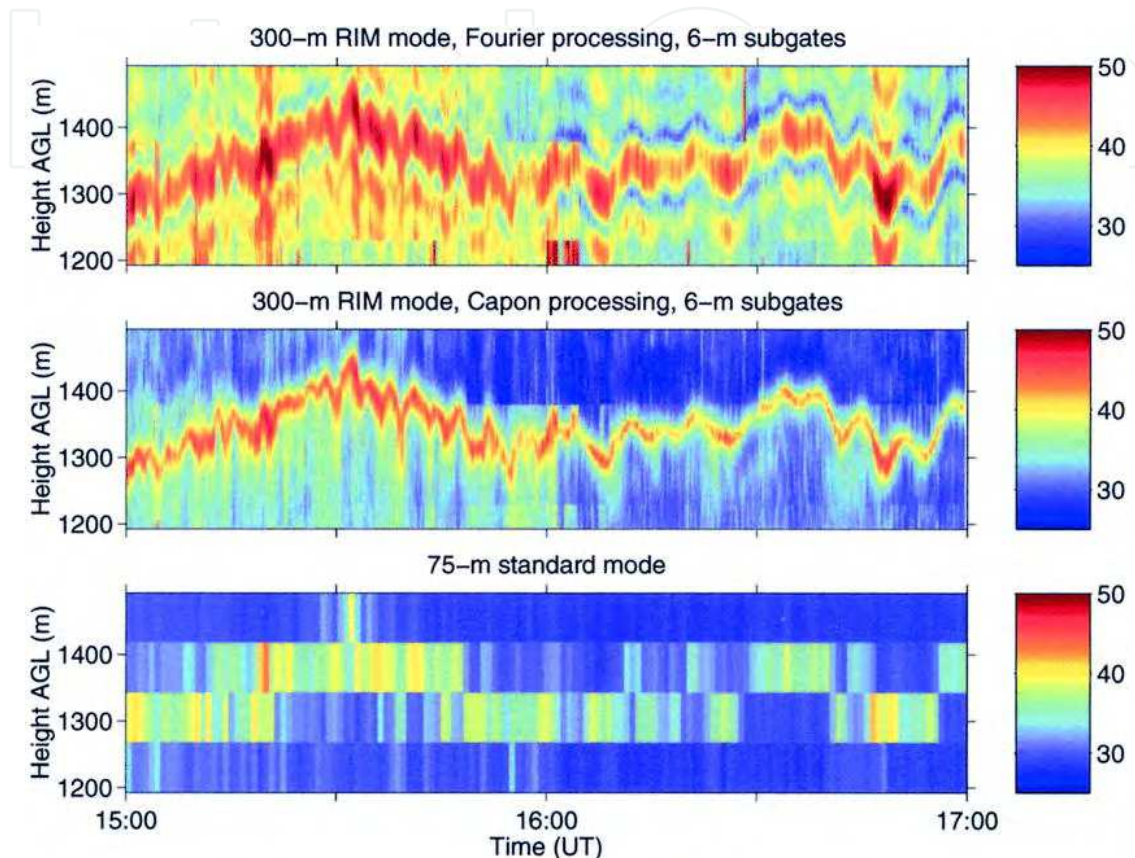
In order to demonstrate that RIM is useful for improving range resolution, measurement results are presented. Fig. 5 shows an example of RIM measurement. The brightness profiles were produced with 6-m range intervals by applying RIM to received signals measured with the 2- μ s transmitted pulse and four transmitted frequencies (914.0, 914.33, 915.33, and 916 MHz). The bandwidth of the RIM measurement was 2.5-MHz (2 MHz for the actual frequency spread and 0.5 MHz for the 2- μ s transmitted pulse). During the experiment, the RIM measurement and single frequency measurement using the 0.5- μ s transmitted pulse (i.e., corresponding to 75-m range resolution and 2-MHz bandwidth) were carried out alternatively. Although the frequency bandwidth difference between the two observation modes was as small as 500 kHz, it is clear that both the brightness produced by the Fourier-based method and by the Capon method show finer height variations than the backscattered power measured with the 75-m range resolution. Further, it is clear that the Capon method attains finer range resolution than the Fourier-based method. By applying RIM to the same dataset, Chilson et al. (2004) produced Doppler velocity with 15-m range intervals and showed that the Doppler velocity produced by RIM agreed well with that measured with the 0.5- μ s transmitted pulse.

Fig. 6 shows an example of Kelvin-Helmholtz (KH) instability (i.e., shear instability) measured by the MU radar operated with a RIM observation mode (Fukao et al., 2011). The measurement was carried out using the new MU radar system upgraded in 2004 (Hassenpflug et al., 2008). Structure of KH billows is clearly seen in the brightness around 1.5 km from 00:35 to 00:53 (Fig. 6a). The resemblance to the evolution of KH vortices measured in the laboratory experiment (Patterson et al., 2006) is striking. Vertical wind velocity shows perturbations with magnitudes of 1 m s⁻¹ or more. Because accurate high-resolution vertical wind measurement is quite difficult for instruments other than clear-air Doppler radars (e.g., Fukao, 2007; Hocking 2011), measurements by wind profiling radars are indispensable to understand turbulence processes in the atmosphere. RIM measurements have revealed a fine structure of KH billows in the jet stream in the mid-latitudes (Luce et al., 2008) and upper-tropospheric easterly jet in the tropical region (Mega et al., 2010). Fukao et al (2011) carried out a statistical analysis of KH billows in order to quantify their occurrence frequency, spatial scales, energy dissipation rate, and vertical eddy diffusivity.

2.2.3 Advantage of range resolution enhancement using multiple frequencies

In the section, advantages of RIM over other methods are described. Radar range resolution is determined by the transmitted pulse width, and ranges typically a hundred to several hundreds of meters. However, for UHF wind profilers, a range resolution down to approximately 30 m is able to be attained by transmitting shorter pulses (e.g., Wilson et al., 2005). Although the range resolution is able to be improved by transmitting shorter pulses, it requires not only wider bandwidth but also more transmitted power in order to keep the

receiver sensitivity constant. RIM also contributes to efficient usage of frequencies. Chilson et al. (2003) pointed out that for the RIM measurement shown in Fig. 5, the spurious intensity of frequency power spectrum of transmitted pulses was smaller than the 0.4- μ s transmitted pulse width which also uses 2.5-MHz bandwidth (see their Fig. 2). RIM is especially useful for VHF wind profiler radars because their frequency bandwidth allowed by license and that determined by antenna are limited.



©American Meteorological Society. Reprinted with permission.

Fig. 5. Time-range plot of (top) brightness produced by the Fourier-based method, (center) brightness produced by the Capon method, and (bottom) backscattered power expressed in decibels (Chilson et al., 2003). The data was collected with the Platville 915-MHz tropospheric wind profiler. See text for details of the measurement.

Pulse compression using frequency-modulated continuous wave (FMCW) is also useful for UHF clear-air radars to improve their range resolution down to several meters or less (Eaton et al., 1995; Richter, 1969). However, a use of the FMCW pulse compression causes deterioration in data quality by range aliasing and by range ambiguity caused by Doppler shift of scatterers. Though range resolution in RIM depends on range distribution of scatterers, signal-to-noise ratio, and signal processing method used for RIM (e.g., Palmer et al., 1999; Luce et al., 2001; Smaïni et al., 2002), RIM does not suffer the drawbacks of using short transmitted pulse or FMCW pulse compression.

RIM contributes to reduce amount of on-line data size and computational complexity. In the case shown in Fig. 5, although the on-line sampling interval of the RIM measurement was 2 μ s (i.e., 300-m range spacing), brightness data are able to be processed with finer (6-m) range

spacing by off-line signal processing. On the other hand, on-line sampling interval in cases of short pulse transmission must be equivalent or shorter compared with the range resolution determined by transmitted pulse width. On-line sampling interval in cases of FMCW transmission also must be equivalent or shorter compared with the range resolution determined by sweep range of transmitted frequency.

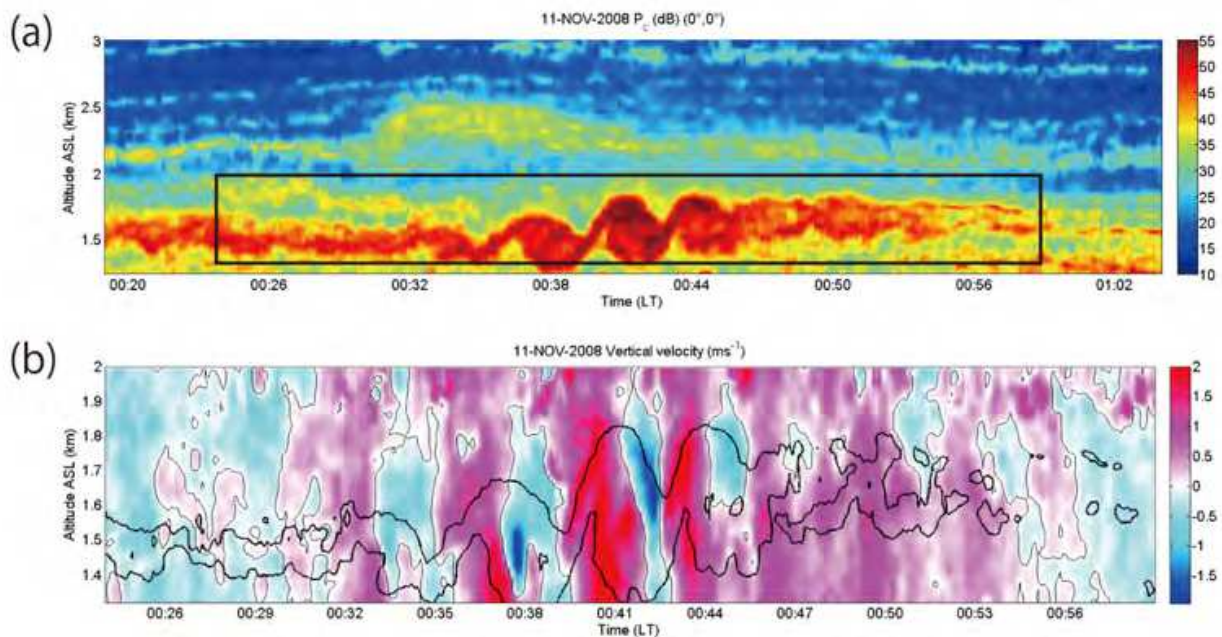


Fig. 6. Time-altitude plots of (a) brightness and (b) vertical wind velocity. Data were collected using vertically-pointing beam of the MU radar operated with the RIM observation mode (Fukao et al., 2011). The region within the black rectangular is plotted in panel (b). The thick black contours in panel (b) show 46 dB brightness level. The figure is reproduced with permission from the Royal Meteorological Society.

2.3 Further applications

2.3.1 High-resolution measurement using both spaced antennas and multiple frequencies

By using spaced receivers and multiple frequencies simultaneously, radar resolution is able to be improved both in angle and range, which leads to realize a three-dimensional (3-D) imaging. Signal processing procedures of the 3-D imaging are described by Yu & Palmer (2001). In 2004, the MU radar was upgraded for the 3-D imaging capability with 5 frequencies across a 1 MHz bandwidth and 25 intermediate frequency (IF) digital receivers (Hassenpflug et al., 2008). Using the 3-D imaging with the Capon method, Hassenpflug et al. (2008) showed a 3-D structure of radar echoes associated with billows of KH instability. Chen et al. (2008) applied the 3-D imaging to data collected by the MU radar in order to investigate relations between the angular distribution of clear-air echo power and tilted refractive-index layers caused by KH instability. The 3-D imaging technique is also able to be used for clutter mitigation. Using the MU radar, Yu et al. (2010) showed that the 3-D imaging provides comparable or better performance of both echo layer reconstruction and clutter mitigation compared to RIM.

The 3-D imaging technique is able to contribute to high-range-resolution wind measurement. Yu and Brown (2004) proposed a technique named RIM-SA that calculates wind velocity using both spaced antennas and multiple frequencies. In RIM-SA, first, RIM was separately applied to signals received by each of spaced antennas in order to produce high-range-resolution received signals. Next, SA technique was applied to the received signals produced by RIM in order to calculate horizontal wind velocity with high range resolution. Using data measured by MAPR, Yu and Brown (2004) produced profiles of horizontal wind velocity with 100-m intervals from a RIM-SA measurement using 2- μ s transmitted pulse and four frequencies (914.667, 915.000, 916.000, and 916.667 MHz). Yu and Brown (2004) showed that the horizontal wind produced by RIM-SA agrees well with both wind velocity measured by a radiosonde and that measured by MAPR using the 0.67- μ s transmitted pulse (i.e., 100-m range resolution).

2.3.2 Assessment of wind velocity measurement

Because DBS has been widely used for wind profiling radars, accuracy of wind velocity measured by DBS needs to be assessed. High resolution measurements using CRI and RIM provide the opportunity to assess the accuracy of wind velocity measured by DBS.

Wind field inhomogeneity within the scanning area of radar beams is a significant factor that produces errors of wind velocity measured by DBS. Cheong et al. (2008) carried out CRI measurement using TEP in order to obtain radial Doppler velocities from 490 beam directions, and used the radial Doppler velocity data in order to estimate how the wind field inhomogeneity affects the error of wind velocity measured by DBS. Cheong et al. (2008) concluded that optimal zenith angle of off-vertical radar beams is approximately 9-10° for minimizing the root-mean square (RMS) error in wind velocity measured by DBS, and that increasing number of off-vertical radar beams significantly reduces the RMS error in wind velocity measured by DBS.

Tilted refractive-index layers caused by KH instability deteriorate the measurement accuracy of vertical wind velocity because the tilted refractive-index layers cause contamination of horizontal wind velocity to the Doppler velocity of vertically-pointed radar beam, from which vertical wind is calculated in DBS (Muschinski, 1996; Yamamoto et al., 2003). Chen et al. (2008) applied the 3-D imaging to data collected by the MU radar in order to investigate relations between angular distribution of clear-air echo power and Doppler velocity measured by the vertically-pointed radar beam with improved range resolution. Chen et al. (2008) successfully showed the clear relation between the Doppler velocity bias measured by the vertically-pointed radar beam and the tilt of radar echo layers.

Though multistatic radar technique is not CRI, it is useful for measuring 3-D distribution of wind velocities. By installing two receiver arrays at approximately 1 km away from the westward and southward of the main antenna of the EAR, Nishimura et al. (2006) and (2010) realized the multistatic radar measurement of wind velocities. Their measurement results revealed 3-D wind perturbations down to the horizontal scale of 500 m.

2.3.3 High-resolution temperature measurement

Radio acoustic sounding system (RASS) is a radar remote sensing system for measuring profiles of temperature¹ with high time and height resolutions (e.g., May et al., 1990; Tsuda et al., 1989). RASS is also able to be used for monitoring humidity profiles (e.g., Furumoto et al., 2005; Tsuda et al., 2001). Using the MU radar, Furumoto et al. (2011) applied RIM to RASS measurement (RIM-RASS) in order to demonstrate that range resolution of temperature is improved down to approximately 60 m compared with the nominal range gate width of 150 m determined by the transmitted pulse width. Furumoto et al. (2011) pointed out that (1) sample time difference at an arbitrary range among data on different operational frequencies and (2) the Doppler shift bias due to the shape of range-gate weighting have to be corrected for RIM-RASS measurement, and developed an iteration algorithm that corrects (1) and (2). By applying CRI to temperature profiles measured by TEP with RASS, Dekker & Frasier (2004) retrieved virtual temperature structure function from horizontal distribution of temperature. The study by Dekker & Frasier (2004) indicates a usefulness of CRI to quantify turbulence intensity in the atmosphere.

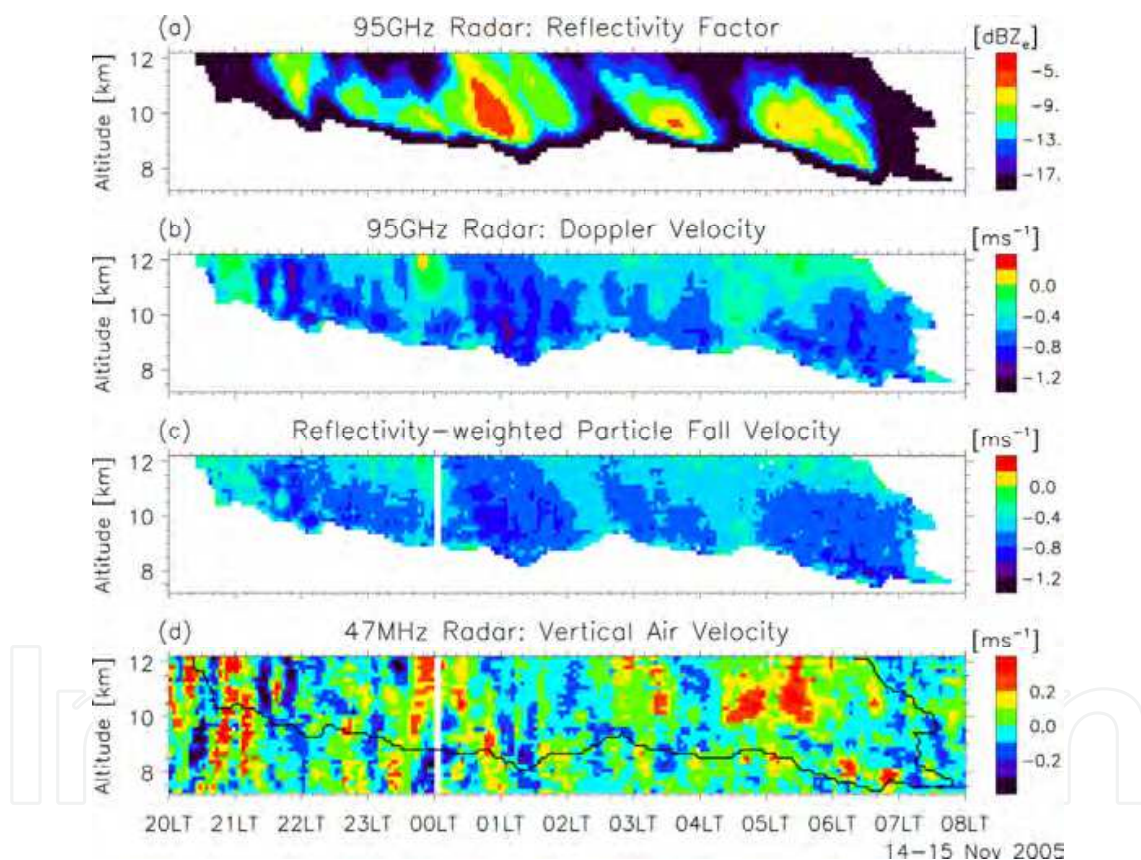


Fig. 7. Time-altitude plot of (a) equivalent radar reflectivity factor, (b) reflectivity-weighted particle fall velocity relative to the ground, (c) reflectivity-weighted particle fall velocity relative to the air, and (d) vertical wind velocity (Yamamoto et al., 2008). Equivalent radar reflectivity factor and reflectivity-weighted particle fall velocity relative to the ground were measured by a millimeter-wave radar. Vertical wind velocity was measured by the EAR. Horie et al. (2000) describe details of the millimeter-wave radar.

¹To be exact, RASS measures a virtual temperature expressed by $T_v = T(1 + 0.61q)$, where T_v , T , and q are virtual temperature in K, temperature in K, and water vapor mixing ratio in kg kg⁻¹, respectively.

3. Multi-instrument measurements

Measurements using collocated wind profiling radar and millimeter-wave radar/lidar have been carried out in the last decade. In section 3, we focus on measurement results of vertical wind in and around clouds due to the following reasons. First, measurement of vertical wind in cloudy region with high resolution and accuracy is difficult by means other than wind profiling radars (e.g., Nishi et al., 2007). Though wind profiling radars measure only the area right above the radars, they are suitable for measuring wind motions with high time and vertical resolutions. Second, observations aiming at clarifying generation and maintenance mechanisms of clouds are indispensable. Clouds reflect a fraction of the solar radiation that would otherwise be absorbed at the Earth's surface. On the other hand, clouds also contribute to the blocking of outgoing radiation by the atmosphere (Wallace and Hobbs, 2006). However, the effects of clouds on the radiation budget of the earth-atmosphere system are not sufficiently quantified (Stephens, 2005). Measurements using collocated wind profiling radar and millimeter-wave radar/lidar provide an opportunity to observe dynamical and microphysical processes of clouds simultaneously.

3.1 Particle fall velocity

Fall velocity of cloud particles (hereafter particle fall velocity) is one of crucial factors that determine life time of clouds (e.g., Petch et al., 1997; Starr and Cox, 1985), and particle fall velocity relative to the air has been modeled in order to relate particle fall velocity to the size and shape of particles [e.g., Heymsfield & Iaquinta, 2000; Mitchell 1996; Mitchell and Heymsfield, 2005]. However, because fall velocity of cloud particles relative to the ground (i.e., a sum of particle fall velocity relative to the air and vertical wind velocity) is measured by millimeter-wave radars or lidars, measurement of vertical wind velocity is required to retrieve particle fall velocity relative to the air. Fig. 7 shows a measurement example. Reflectivity-weighted particle fall velocity relative to the ground, which was measured by a millimeter-wave radar, showed small-scale perturbations with a time scale less than several ten minutes (Fig. 7b). The small-scale perturbations were caused by vertical wind motions (Fig. 7d). By subtracting vertical wind velocity from the reflectivity-weighted particle fall velocity relative to the ground, reflectivity-weighted particle fall velocity relative to the air was retrieved (Fig. 7c). The small-scale perturbations caused by the vertical wind motions were not observed in the retrieved reflectivity-weighted particle fall velocity relative to the air. The results clearly demonstrate that vertical wind measurement by wind profiling radar is useful for measuring particle fall velocity accurately. Retrieval of particle fall velocity leads to data analysis to clarify cloud properties. Using data shown by Figs. 7a and c, Yamamoto et al. (2008) related particle fall velocity to cloud particle size. The collected data were also used to assess an algorithm that retrieves vertical wind velocity, effective diameter of cloud particles, and ice water content from millimeter-wave radar and lidar measurements (Sato et al., 2009). Using the MU radar and an X-band Doppler weather radar (Yamamoto et al., 2011a), Luce et al. (2010a) showed a similar retrieval result of particle fall velocity (see their Fig. 15).

3.2 Turbulence measurements in and around clouds

Fig. 8 presents a measurement result around the cloud bottom. Cloud bottom altitude estimated by the equivalent radar reflectivity factor showed protuberance structure. Such

protuberances are referred to as mammatus cloud, whose generation mechanisms still remain to be discussed (Schultz et al., 2006). Brightness showed an increase around the cloud border due to the turbulence generation by KH instability. Vertical wind velocity showed oscillations exceeding $\pm 3 \text{ m s}^{-1}$ in magnitude due to KH instability, and played a role in producing protuberances of clouds through its downward motions. Luce et al. (2010a) suggested that the reduction of static stability at the interface between the clear air and cloud provided the favorable condition for triggering KH instabilities. Using the MU radar and a lidar (Behrendt et al., 2004), Luce et al. (2010b) also showed a correspondence between protuberances of clouds and vertical wind disturbances caused by atmospheric instability. Using the MU radar and a scanning millimeter-wave radar (Hamazu et al., 2003), Wada et al. (2005) showed a 3-D cell structure of cirrus clouds generated by KH instability, and the cell structures have greater vertical extension in the presence of upward vertical wind.

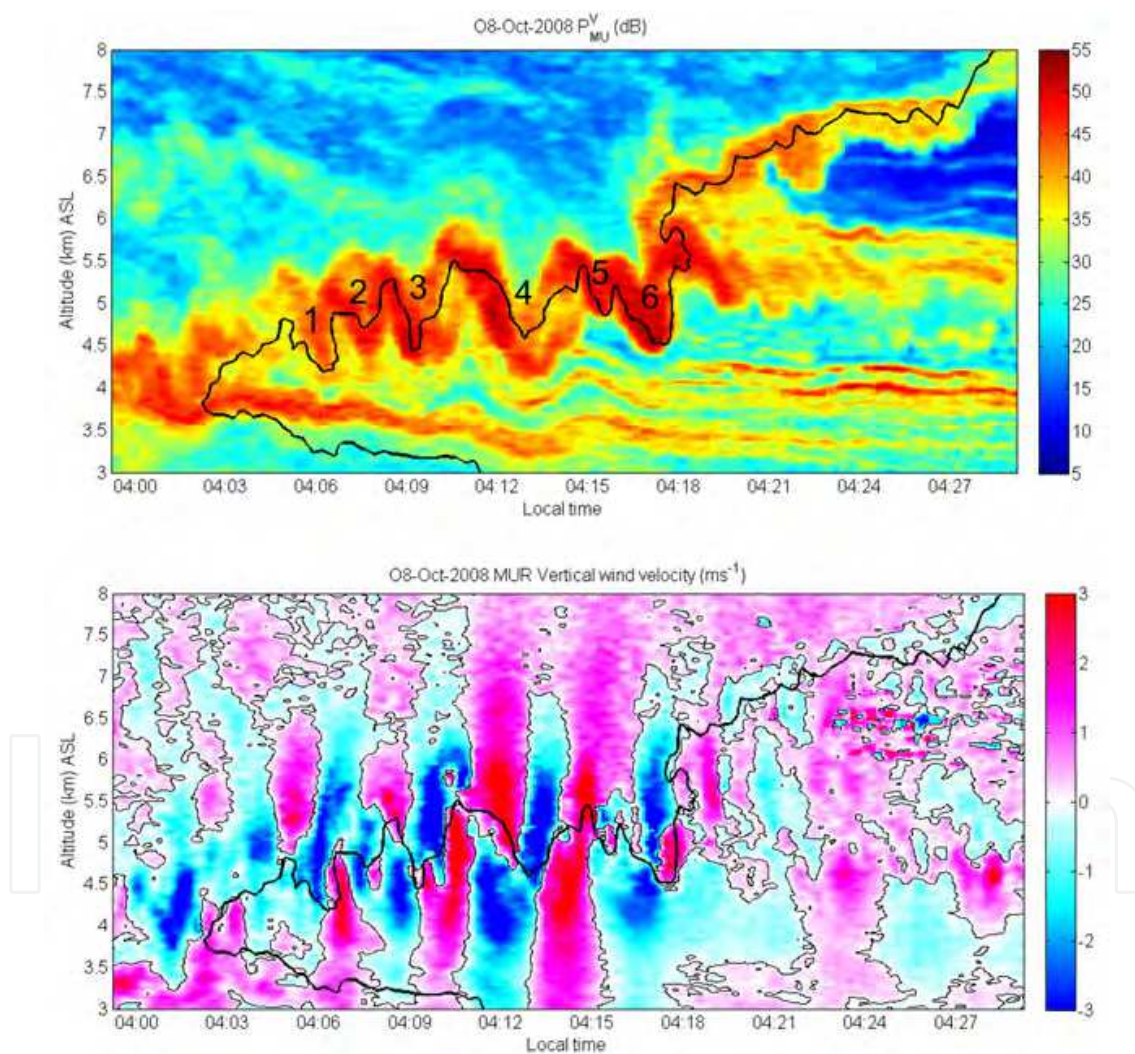


Fig. 8. Time-altitude plot of (upper) brightness and (lower) vertical wind velocity measured by the vertical beam of the MU radar operated with the RIM measurement mode (Luce et al., 2010a). Thick black curve shows a contour of -6 dB_{ze} equivalent radar reflectivity factor measured by a millimeter-wave radar. Numbers 1-6 shown in the upper panel indicate protuberances of clouds. Yamamoto et al. (2011b) describe details of the millimeter-wave radar.

Fig. 9 shows a measurement result around the cloud top. In the upper part of clouds, an increase of spectral width up to $0.5\text{--}0.7\text{ m s}^{-1}$, which indicates the presence of small-scale turbulence triggered by convective instabilities, is observed (Fig. 9c). Further, in the top part of clouds (0–500 m below the cloud tops), downward wind up to $0.2\text{--}0.3\text{ m s}^{-1}$, which was caused by radiative cooling, was observed. For further discussion on the generation mechanism of turbulence, see Yamamoto et al. (2009a). From a case study using data measured by the MU radar and Raman/Mie lidar, Yamamoto et al. (2009b) showed a clear relation between the cloud-top altitude of mid-latitude cirrus and the bottom altitude of subtropical jet with high time and altitude resolutions (12 min and 150 m, respectively).

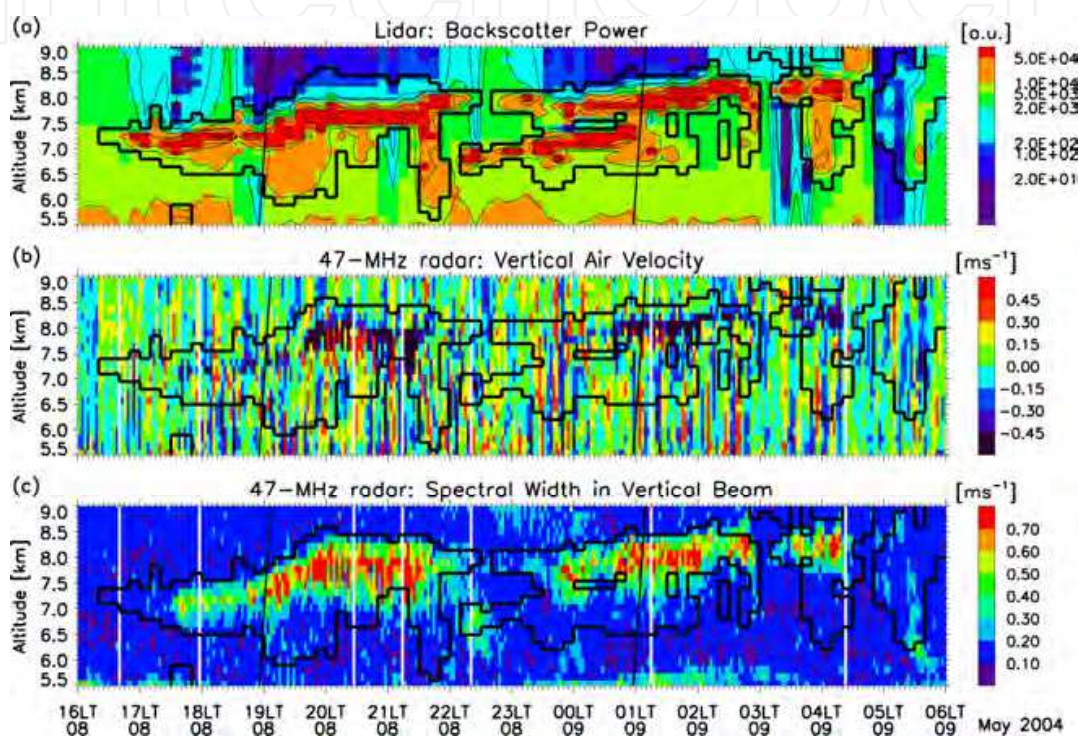


Fig. 9. Time-altitude plots of (a) backscattered power measured by a 532-nm Mie lidar, and (b) vertical wind velocity and (c) spectral width measured by the vertical beam of the EAR (Yamamoto et al., 2009a). Thick black curves in each panel indicate cloud boundaries estimated by the lidar backscattered power.

3.3 Other measurements

Measurements using wind profiling radars and other instruments are not limited to cloud researches. Measurement results of stratosphere-troposphere exchange (STE) processes have been reported in the last decade. Using observation network of wind profiling radar and lidar, Bertin et al. (2001) showed details of turbulent generation above and below the jet axis associated with a tropopause folding in the middle latitude. Using measurement data collected by the MU radar and ozonesonde, Gavrilov et al. (2006) compared distribution of turbulent diffusivity with vertical ozone flux. It is well known that clear-air echo power showed a vertical increase around the tropopause due to the increase of static stability or turbulence intensity (see section 14 of Hocking, 2011). Using data collected by the intensive observation of wind profiling radars and ozonesonde at Canada, Hocking et al. (2007) showed that stratospheric ozone has impacts on tropospheric ozone by its downward

transportation to the ground, and demonstrated that tropopause altitude determined by wind profiling radar with high time resolution can be used to infer the possibility of ozone intrusions, as well as to represent tropopause motions in association with stratosphere-troposphere transport. Using the EAR and radiosondes, Fujiwara et al. (2003) showed the turbulence generation around the tropical tropopause caused by the Kelvin wave breaking.

Using results of RIM measurement by the MU radar and water vapor measurement by the Raman lidar (Behrendt, et al., 2004), Luce et al. (2010c) demonstrated that vertical gradient of humidity causes enhancement of backscattered intensity of radar echo by generating refractive index irregularities at the Bragg scale. Further coordinated observations would lead to clarify the radio scattering and propagation mechanisms in the clear air.

4. Conclusion

In the Chapter, new observations by wind profiling radars in the last decade were reviewed. In section 2, the signal processing and measurement results of radar interferometry techniques (CRI and RIM) were described. Resolution enhancements attained by CRI and RIM will be useful not only for scientific researches aiming at clarifying atmospheric processes but also practical radar utilization through improvement in data quality (i.e., clutter mitigation) and early detection of turbulence associated with storm or wind shear. Further assessments aiming at quantifying their usefulness under various weather conditions are desirable.

In section 3, it was demonstrated that multi-instrument measurement using wind profiling radar and millimeter-wave radar/lidar is useful to clarify phenomena related to cloud processes. In order to clarify interactions among dynamics, cloud physics, and radiation, simultaneous remote sensing and in-situ measurements are highly desirable. In-situ measurements of cloud particles, temperature, humidity, and radiation using balloons and/or aircrafts will contribute to quantify phenomena measured by wind profiling radar, millimeter-wave radar, and lidar. Numerical simulation is also important to assess the interactions. The author hopes that efforts to realize further coordinated studies are executed continuously.

5. Acknowledgment

This work was supported by the research grant for Exploratory Research on Sustainable Humanosphere Science from Research Institute for Sustainable Humanosphere (RISH), Kyoto University.

6. References

- Behrendt, A., Nakamura, T. & Tsuda, T. (2004). Combined Temperature Lidar for Measurements in the Troposphere, Stratosphere, and Mesosphere, *Applied Optics*, Vol. 43, No.14, pp.2930-2939, doi:10.1364/AO.43.002930.
- Bertin, F., Campistron, B., Caccia, J.L. & Wilson, R. (2001). Mixing Processes in a Tropopause Folding Observed by a Network of ST Radar and Lidar, *Annales Geophysicae*, Vol.19, No.8, pp.953-963, doi:10.5194/angeo-19-953-2001.

- Capon, J. (1969). High-Resolution Frequency-Wavenumber Spectrum Analysis, *Proceedings of the IEEE*, Vol.57, No.8, pp.1408 -1418, doi:10.1109/PROC.1969.7278.
- Chau, J.L. & Woodman, R.F. (2001). Three-Dimensional Coherent Radar Imaging at Jicamarca: Comparison of Different Inversion Techniques, *Journal of Atmospheric and Solar-Terrestrial Physics*, Vol.63, No.2-3, pp.253-261, doi:10.1016/S1364-6826(00)00142-5.
- Chen, J.-S. (2004). On the Phase Biases of Multiple-frequency Radar Returns of Mesosphere-Stratosphere-Troposphere Radar, *Radio Science*, Vol.39, Art.no.RS5013, doi:10.1029/2003RS002885.
- Chen, J.-S., Hassenpflug, G. & Yamamoto, M. (2008). Tilted Refractive-index Layers Possibly Caused by Kelvin-Helmholtz Instability and Their Effects on the Mean Vertical Wind Observed with Multiple-receiver and Multiple-frequency Imaging Techniques, *Radio Science*, Vol.43, Art.no.RS4020, doi:10.1029/2007RS003816.
- Chen, J.-S., Su, C.-L., Chu, Y.-H., Hassenpflug, G. & Zecha, M. (2009). Extended Application of a Novel Phase Calibration Approach of Multiple-Frequency Range Imaging to the Chung-Li and MU VHF Radars. *Journal of Atmospheric and Oceanic Technology*, Vol.26, No.11, pp.2488-2500, doi:10.1175/2009JTECHA1295.1.
- Chen, J.-S. & Zecha, M. (2009). Multiple-Frequency Range Imaging Using the OSWIN VHF Radar: Phase Calibration and First Results, *Radio Science*, Vol.44, Art.No.RS1010, doi:10.1029/2008RS003916.
- Chen, J.-S., Furumoto, J.-I. & Nakamura, T. (2010). Effects of Radar Beam Width and Scatterer Anisotropy on Multiple-Frequency Range Imaging Using VHF Atmospheric Radar, *Radio Science*, Vol.45, Art.no.RS5001, doi:10.1029/2009RS004267.
- Chen, M.-Y., Yu, T.-Y., Chu, Y.-H., Brown, W.O.J. & Cohn, S.A. (2007). Application of Capon Technique to Mitigate Bird Contamination on a Spaced Antenna Wind Profiler, *Radio Science*, Vol.42, Art.no.RS6005, doi:10.1029/2006RS003604.
- Cheong, B.L., Hoffman, M.W., Palmer, R.D., Frasier, S. J. & López-Dekker, F.J. (2004). Pulse Pair Beamforming and the Effects of Reflectivity Field Variations on Imaging Radars, *Radio Science*, Vol.39, RS3014, doi:10.1029/2002RS002843.
- Cheong, B.L., Hoffman, M.W., Palmer, R.D., Frasier, S.J. & López-Dekker, F.J. (2006). Phased-Array Design for Biological Clutter Rejection: Simulation and Experimental Validation, *Journal of Atmospheric and Oceanic Technology*, Vol.23, No4, .pp.585-598, doi:10.1175/JTECH1867.1.
- Cheong, B.L., Palmer, R.D., Yu, T.-Y., Yang, K-F., Hoffman, M.W., Frasier, S.J. & Lopez-Dekker F.J. (2008). Effects of Wind Field Inhomogeneities on Doppler Beam Swinging Revealed by an Imaging Radar, *Journal of Atmospheric and Oceanic Technology*, Vol.25, No.8, pp.1414-1422, doi:10.1175/2007JTECHA969.1.
- Chilson, P.B., Yu, T.-Y., Strauch, R.G., Muschinski, A. & Palmer, R.D. (2003). Implementation and Validation of Range Imaging on a UHF Radar Wind Profiler, *Journal of Atmospheric and Oceanic Technology*, Vol.20, No.7, pp.987-996, doi:10.1175/1520-0426(2003)20<987:IAVORI>2.0.CO;2.
- Chilson, P.B. (2004). The Retrieval and Validation of Doppler Velocity Estimates from Range Imaging. *Journal of Atmospheric and Oceanic Technology*, Vol.21, No.7, pp.1033-1043, doi:10.1175/1520-0426(2004)021<1033:TRAVOD>2.0.CO;2.

- Dekker, P.L. & Frasier, S.J. (2004). Radio Acoustic Sounding with a UHF Volume Imaging Radar. *Journal of Atmospheric and Oceanic Technology*, Vol.21, No.5, pp.766-776, doi:10.1175/1520-0426(2004)021<0766:RASWAU>2.0.CO;2.
- Eaton, F.D., McLaughlin, S.A. & J. R. Hines (1995). A New Frequency-Modulated Continuous Wave Radar for Studying Planetary Boundary Layer Morphology, *Radio Science*, Vol.30, No.1, pp.75-88, doi:10.1029/94RS01937.
- Fujiwara, M., Yamamoto, M.K., Hashiguchi, H., Horinouchi, T. & Fukao, S. (2003). Turbulence at the Tropopause due to Breaking Kelvin Waves Observed by the Equatorial Atmosphere Radar, *Geophysical Research Letters*, Vol.30, No.4, 1171, doi:10.1029/2002GL016278.
- Fukao, S., Sato, T., Tsuda, T., Yamamoto, M., Yamanaka, M.D. & Kato, S. (1990). MU radar: New Capabilities and System Calibrations, *Radio Science*, Vol.25, No.4, doi:10.1029/RS025i004p00477.
- Fukao, S., Hashiguchi, H., Yamamoto, M., Tsuda, T., Nakamura, T., Yamamoto, M. K., Sato, T., Hagio, M. & Yabugaki, Y. (2003). Equatorial Atmosphere Radar (EAR): System Description and First Results, *Radio Science*, Vol.38, Art.No.1053, doi:10.1029/2002RS002767.
- Fukao, S. (2007) Recent Advances in Atmospheric Radar Study, *Journal of the Meteorological Society of Japan*, Vol.85B, pp.215-239, doi:10.2151/jmsj.85B.215.
- Fukao, S., Luce, H., Mega, T. & Yamamoto, M.K. (2011), Extensive Studies of Large-Amplitude Kelvin-Helmholtz Billows in the Lower Atmosphere with the VHF Middle and Upper Atmosphere radar (MUR), *Quarterly Journal of the Royal Meteorological Society*, Vol.137, No.657, 1019-1041, doi:10.1002/qj.807.
- Furumoto, J.-I., Iwai, S., Fujii, H., Tsuda, T., Xin, W., Koike, T. & Bian L. (2005). Estimation of Humidity Profiles with the L-Band Boundary Layer Radar-RASS Measurements, *Journal of the Meteorological Society of Japan*, Vol.83, No.5, pp.895-908, doi:10.2151/jmsj.83.895.
- Furumoto, J.-I., Shinoda, T., Matsugatani, A. & Tsuda T (2011). Measurements of Detailed Temperature Profiles within the Radar Range Gate Using the Range Imaging Technique, *Journal of Atmospheric and Oceanic Technology*, Vol.28, No.1, pp.22-36, doi:10.1175/2010JTECHA1506.1.
- Gage, K.S. (1990). Radar Observations of the Free Atmosphere: Structure and Dynamics, In : *Radar in Meteorology*, D. Atlas, (Ed.), pp.534-565, American Meteorological Society, ISBN-10: 0933876866, Boston, Massachusetts, USA.
- Gavrilov, N. M., Fukao, S., Hashiguchi, H., Kita, K., Sato, K., Tomikawa, Y. & Fujiwara, M. (2006), Combined MU Radar and Ozonesonde Measurements of Turbulence and Ozone Fluxes in the Tropo-stratosphere over Shigaraki, Japan, *Geophysical Research Letters*, Vol.33, Art.no.L09803, doi:10.1029/2005GL024002.
- Hamazu, K., Hashiguchi H., Wakayama T., Matsuda T., Doviak R. J. & Fukao, S. (2003). A 35-GHz Scanning Doppler Radar for Fog Observations. *Journal of Atmospheric and Oceanic Technology*, Vol.20, No.7, pp.972-986, doi:10.1175/1520-0426(2003)20<972:AGSDRF>2.0.CO;2.
- Hassenpflug, G., Yamamoto, M., Luce, H. & Fukao, S. (2008). Description and Demonstration of the New Middle and Upper Atmosphere Radar Imaging System: 1-D, 2-D, and 3-D Imaging of Troposphere and Stratosphere, *Radio Science*, Vol.43, Art.no.RS2013, doi:10.1029/2006RS003603.

- Héchal, D., Crochet, M., Luce, H. & Spano, E. (2001). Radar Imaging and High-Resolution Array Processing Applied to a Classical VHF-ST Profiler, *Journal of Atmospheric and Solar-Terrestrial Physics*, Vol.63, No.2-3, doi:10.1016/S1364-6826(00)00135-8.
- Heymsfield, A.J. & Iaquinta, J. (2000). Cirrus Crystal Terminal Velocities, *Journal of the Atmospheric Sciences*, Vol.57, No.7, pp.916-938, doi:10.1175/1520-0469(2000)057<0916:CCTV>2.0.CO;2.
- Hocking, W.K. (1985). Measurement of Turbulent Energy Dissipation Rates in the Middle Atmosphere by Radar Techniques: A Review, *Radio Science*, Vol.20, No.6, pp.1403-1422, doi:10.1029/RS020i006p01403.
- Hocking, W.K., Carey-Smith T., Tarasick, D.W., Argall P.S., Strong, K., Rochon, Y., Zawadzki, I. & P. A. Taylor (2007). Detection of Stratospheric Ozone Intrusions by Windprofiler Radars, *Nature*, Vol.450, No.7167, pp.281-284, doi:10.1038/nature06312.
- Hocking, W.K. (2011). A Review of Mesosphere-Stratosphere-Troposphere (MST) Radar Developments and Studies, Circa 1997-2008, *Journal of Atmospheric and Solar-Terrestrial Physics*, Vol.73, No.9, pp.848-882, doi:10.1016/j.jastp.2010.12.009.
- Horie, H., Iguchi, T., Hanado, H., Kuroiwa, H., Okamoto, H. & Kumagai, H. (2000). Development of a 95-GHz Airborne Cloud Profiling Radar (SPIDER) - Technical aspects -, *IEICE Transactions on Communications*, Vol.E83-B, No.9, pp.2010-2020.
- Ishihara, M., Kato, Y., Abo, T., Kobayashi, K. & Izumikawa, Y. (2006). Characteristics and Performance of the Operational Wind Profiler Network of the Japan Meteorological Agency, *Journal of the Meteorological Society of Japan*, Vol.84, No.6, pp.1085-1096, doi:10.2151/jmsj.84.1085.
- Kamio, K., Nishimura, K. & Sato, T. (2004). Adaptive Sidelobe Control for Clutter Rejection of Atmospheric Radars, *Annales Geophysicae*, Vol.22, No.11, pp.4005-4012, doi:10.5194/angeo-22-4005-2004.
- Kollias, P., Clothiaux, E.E., Miller, M.A., Albrecht, B.A., Stephens, G.L. & Ackerman T. P. (2007). Millimeter-Wavelength Radars: New Frontier in Atmospheric Cloud and Precipitation Research, *Bulletin of the American Meteorological Society*, Vol.88, No.10, pp.1608-1624, doi:10.1175/BAMS-88-10-1608.
- Larsen, M.F. & Röttger, J. (1989). The Spaced Antenna Technique for Radar Wind Profiling, *Journal of Atmospheric and Oceanic Technology*, Vol.6, No.6, pp.920-938, doi:10.1175/1520-0426(1989)006<0920:TSATFR>2.0.CO;2.
- Le, K.D., Palmer, R.D., Cheong, B.L., Yu, T.-Y., Zhang, G. & Torres, S.M. (2010). Reducing the Effects of Noise on Atmospheric Imaging Radars Using Multilag Correlation, *Radio Science*, Vol.45, RS1008, doi:10.1029/2008RS003989.
- Luce, H., Yamamoto, M., Fukao, S., Héchal, D. & Crochet M. (2001). A Frequency Domain Radar Interferometric Imaging (FII) Technique Based on High-Resolution Methods, *Journal of Atmospheric and Solar-Terrestrial Physics*, Vol.63, No.2-3, pp.221-234, doi:10.1016/S1364-6826(00)00147-4.
- Luce, H., Hassenpflug, G., Yamamoto, M., Fukao, S. & Sato, K. (2008). High-Resolution Observations with MU Radar of a KH Instability Triggered by an Inertia-Gravity Wave in the Upper Part of a Jet Stream, *Journal of the Atmospheric Sciences*, Vol.65, No.5, pp.1711-1718, doi:10.1175/2007JAS2346.1.
- Luce, H., Mega, T., Yamamoto, M.K., Yamamoto, M., Hashiguchi, H., Fukao, S., Nishi, N., Tajiri, T. & Nakazato, M. (2010a). Observations of Kelvin-Helmholtz Instability at a

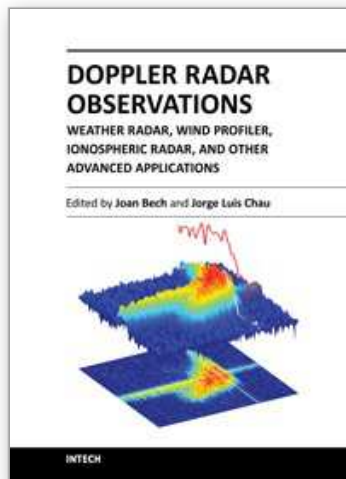
- Cloud Base with the Middle and Upper Atmosphere (MU) and Weather Radars, *Journal of Geophysical Research*, Vol.115, Art.no.D19116, doi:10.1029/2009JD013519.
- Luce, H., Nakamura, T., Yamamoto, M. K., Yamamoto, M. & Fukao, S. (2010b). MU Radar and Lidar Observations of Clear-Air Turbulence Underneath Cirrus, *Monthly Weather Review*, Vol.138, No.2, pp.438-452, doi:10.1175/2009MWR2927.1.
- Luce, H., Takai, T., Nakamura, T., Yamamoto, M., Fukao, S. (2010c). Simultaneous Observations of Thin Humidity Gradients in the Lower Troposphere with a Raman Lidar and the Very High-Frequency Middle- and Upper-Atmosphere Radar, *Journal of Atmospheric and Oceanic Technology*, Vol.27, No. 5, pp.950-956, doi:10.1175/2010JTECHA1372.1.
- May, P.T. (1990). Spaced antenna versus Doppler Radars: A Comparison of Techniques Revisited, *Radio Science*, Vol.25, No.6, pp.1111-1119, doi:10.1029/RS025i006p01111.
- May, P.T., Strauch, R.G., Moran, K.P. & Ecklund, W.L. (1990). Temperature Sounding by RASS with Wind Profiler Radars: A Preliminary Study, *IEEE Transactions on Geoscience and Remote Sensing*, Vol.28, No.1, pp.19-28, doi:10.1109/36.45742.
- Mead, J.B., Hopcraft, G., Frasier, S.J., Pollard, B.D., Cherry, C.D., Schaubert, D.H. & McIntosh, R.E. (1998). A Volume-Imaging Radar Wind Profiler for Atmospheric Boundary Layer Turbulence Studies, *Journal of Atmospheric and Oceanic Technology*, Vol.15, No.4, pp.849-859, doi:10.1175/1520-0426(1998)015<0849:AVIRWP>2.0.CO;2.
- Mega, T., Yamamoto, M.K., Luce, H., Tabata, Y., Hashiguchi, H., Yamamoto, M., Yamanaka, M. D. & Fukao, S. (2010). Turbulence Generation by Kelvin-Helmholtz Instability in the Tropical Tropopause Layer Observed with a 47 MHz Range Imaging Radar, *Journal of Geophysical Research*, Vol.115, Art.no.D18115, doi:10.1029/2010JD013864.
- Met Office (2011), CWINDE Network, Available from <http://www.metoffice.gov.uk/science/specialist/cwinde/>.
- Mitchell, D.L. (1996). Use of Mass- and Area-Dimensional Power Laws for Determining Precipitation Particle Terminal Velocities. *Journal of the Atmospheric Sciences*, Vol.53, No.12, pp.1710-1723, doi:10.1175/1520-0469(1996)053<1710:UOMAAD>2.0.CO;2.
- Mitchell, D.L. & Heymsfield, A.J. (2005). Refinements in the Treatment of Ice Particle Terminal Velocities, Highlighting Aggregates. *Journal of the Atmospheric Sciences*, Vol.62, No.5, pp.1637-1644, doi:10.1175/JAS3413.1.
- Muschinski, A. (1996). Possible Effect of Kelvin-Helmholtz Instability on VHF Radar Observations of the Mean Vertical Wind, *Journal of Applied Meteorology*, Vol.35, No.12, pp.2210-2217, doi:10.1175/1520-0450(1996)035<2210:PEOKHI>2.0.CO;2.
- Nishi, N., Yamamoto, M. K., Shimomai, T., Hamada, A. & Fukao, S. (2007). Fine Structure of Vertical Motion in the Stratiform Precipitation Region Observed by a VHF Doppler Radar Installed in Sumatra, Indonesia, *Journal of Applied Meteorology and Climatology*, Vol.46, No.4, pp.522-537, doi:10.1175/JAM2480.1.
- Nishimura, K., Gotoh, E. & Sato, T. (2006). Fine Scale 3D Wind Field Observation with a Multistatic Equatorial Atmosphere Radar, *Journal of the Meteorological Society of Japan*, Vol.84A, pp.227-238, doi:10.2151/jmsj.84A.227.
- Nishimura, K., Harada, T. & Sato, T. (2010). Multistatic Radar Observation of a Fine-Scale Wind Field with a Coupling-Compensated Adaptive Array Technique, *Journal of the Meteorological Society of Japan*, Vol.88, No.3, pp.409-424, doi:10.2151/jmsj.2010-309.

- Palmer, R.D., Gopalam, S., Yu, T.-Y. & Fukao S. (1998). Coherent Radar Imaging Using Capon's Method, *Radio Science*, Vol.33, No.6, pp.1585-1598, doi:10.1029/98RS02200.
- Palmer, R.D., Yu, T.-Y. & Chilson, P. B. (1999). Range Imaging Using Frequency Diversity, *Radio Science*, Vol.34, No.6, pp.1485-1496, doi:10.1029/1999RS900089.
- Palmer, R.D., Chilson, P.B., Muschinski, A., Schmidt, G., Yu, T.-Y. & Steinhagen H. (2001). SOMARE-99: Observations of Tropospheric Scattering Layers Using Multiple-Frequency Range Imaging, *Radio Science*, Vol.36, No.4, pp.681-693, doi:10.1029/1999RS002307.
- Palmer, R.D., Cheong, B.L., Hoffman, M.W., Frasier, S.J., López-Dekker, F.J. (2005). Observations of the Small-Scale Variability of Precipitation Using an Imaging Radar. *Journal of Atmospheric and Oceanic Technology*, Vol.22, No.8, pp.1122-1137, doi:10.1175/JTECH1775.1.
- Patterson, M.D., Caulfield, C.P., McElwaine, J.N. & Dalziel, S.B. (2006). Time-dependent Mixing in Stratified Kelvin-Helmholtz Billows: Experimental Observations, *Geophysical Research Letters*, Vol.33, Art.no.L15608, doi:10.1029/2006GL026949.
- Petch, J.C., Craig, G.C. & Shine, K.P. (1997). A Comparison of Two Bulk Microphysical Schemes and Their Effects on Radiative Transfer Using a Single column Model, *Quarterly Journal of the Royal Meteorological Society*, Vol.123, No.542, pp.1561-1580, doi:10.1002/qj.49712354206.
- Pollard, B.D., Khanna, S., Frasier, S.J., Wyngaard, J.C., Thomson, D.W., & McIntosh, R.E. (2000). Local Structure of the Convective Boundary Layer from a Volume-Imaging Radar, *Journal of the Atmospheric Sciences*, Vol.57, No.15, pp.2281-2296, doi:10.1175/1520-0469(2000)057<2281:LSOTCB>2.0.CO;2.
- Richter, J.H. (1969). High Resolution Tropospheric Radar Sounding, *Radio Science*, Vol.4, No.12, pp.1261-1268, doi :10.1029/RS004i012p01261.
- Sato, K. & Coauthors (2009). 95-GHz Doppler Radar and Lidar Synergy for Simultaneous Ice Microphysics and in-cloud Vertical Air Motion Retrieval, *Journal of Geophysical Research*, Vol.114, Art.no.D03203, doi:10.1029/2008JD010222.
- Schultz, D. M. & Coauthors (2006). The Mysteries of Mammatus Clouds: Observations and Formation Mechanisms. *Journal of the Atmospheric Sciences*, Vol.63, No.10, pp.2409-2435, doi:10.1175/JAS3758.1.
- Smaïni, L., Luce, H., Crochet, M. & Fukao, S. (2002). An Improved High-Resolution Processing Method for a Frequency Domain Interferometric Imaging (FII) Technique. *Journal of Atmospheric and Oceanic Technology*, Vol.19, No.6, pp.954-966, doi:10.1175/1520-0426(2002)019<0954:AIHRPM>2.0.CO;2.
- Stanley G.B., Schwartz, B.E., Koch, S.E., & Szoke, E.J. (2004). The Value of Wind Profiler Data in U.S. Weather Forecasting, *Bulletin of the American Meteorological Society*, Vol.85, No.12, pp.1871-1886, doi:10.1175/BAMS-85-12-1871.
- Starr, D. O'C. & Cox, S.K. (1985). Cirrus Clouds. Part II: Numerical Experiments on the Formation and Maintenance of Cirrus, *Journal of the Atmospheric Sciences*, Vol.42, No.23, pp.2682-2694, doi:10.1175/1520-0469(1985)042<2682:CCPINE>2.0.CO;2.
- Stephens, G.L. (2005). Cloud Feedbacks in the Climate System: A Critical Review, *Journal of Climate*, Vol.18, No.2, pp.237-273, doi:10.1175/JCLI-3243.1.
- Tsuda, T. and Coauthors (1989). High Time Resolution Monitoring of Tropospheric Temperature with a Radio Acoustic Sounding System (RASS), *Pure and Applied Geophysics*, Vol.130, No.2-3, pp.497-507, doi:10.1007/BF00874471.

- Tsuda, T., Miyamoto, M. & Furumoto, J.-I. (2001). Estimation of a Humidity Profile Using Turbulence Echo Characteristics, *Journal of Atmospheric and Oceanic Technology*, Vol.18, No.7, pp.1214-1222, doi:10.1175/1520-0426(2001)018<1214:EOAHPU>2.0.CO;2.
- Vaughn, C.R. (1985). Birds and Insects as Radar Targets: A Review, *Proceedings of the IEEE*, Vol.73, No.2, pp. 205 -227, doi:10.1109/PROC.1985.13134.
- Wallace, J.M. & Hobbs P.V. (2006). *Atmospheric Science: An Introductory Survey, 2nd Edition*, pp.447-450, Academic Press, ISBN-10: 012732951X, San diego, California, USA.
- Wada, E., Hashiguchi, H., Yamamoto, M.K., Teshiba, M. & Fukao, S. (2005). Simultaneous Observations of Cirrus Clouds with a Millimeter-Wave Radar and the MU Radar, *Journal of Applied Meteorology*, Vol.44, No.3, pp.313-323, doi:10.1175/JAM2191.1.
- Wandinger, U. (2005). Introduction to Lidar, In : *Lidar : Range-Resolved Optical Remote Sensing of the Atmosphere*, C. Weitkamp, (Ed.), pp.1-18, Springer, ISBN-10: 0387400753, New York, USA.
- Wilson, R., Dalaudier, F. & Bertin, F. (2005). Estimation of the Turbulent Fraction in the Free Atmosphere from MST Radar Measurements, *Journal of Atmospheric and Oceanic Technology*, Vol.22, No.9, pp.1326-1339, doi:10.1175/JTECH1783.1.
- Wilczak, J. M. & Coauthors (1995). Contamination of Wind Profiler Data by Migrating Birds: Characteristics of Corrupted Data and Potential Solutions. *Journal of Atmospheric and Oceanic Technology*, Vol.12, No.3, pp.449-467, doi:10.1175/1520-0426(1995)012<0449:COWPDB>2.0.CO;2.
- Woodman, R. (1997). Coherent Radar Imaging: Signal Processing and Statistical Properties, *Radio Science*, Vol.32, No.6, pp.2373-2391, doi:10.1029/97RS02017.
- Yamamoto, M.K., Fujiwara M., Horinouchi, T., Hashiguchi, H. & Fukao S. (2003). Kelvin-Helmholtz Instability around the Tropical Tropopause Observed with the Equatorial Atmosphere Radar, *Geophysical Research Letters*, Vol.30, No.9, Art.no.1476, doi:10.1029/2002GL016685.
- Yamamoto, M.K. & Coauthors (2008). Observation of Particle Fall Velocity in Cirriform Cloud by VHF and Millimeter-Wave Doppler radars, *Journal of Geophysical Research*, Vol.113, Art.no.D12210, doi:10.1029/2007JD009125.
- Yamamoto, M.K. & Coauthors (2009a). Vertical Air Motion in Midlevel Shallow-Layer Clouds Observed by 47-MHz Wind Profiler and 532-nm Mie lidar: Initial Results, *Radio Science*, Vol.44, Art.no.RS4014, doi:10.1029/2008RS004017.
- Yamamoto, M.K. & Coauthors (2009b). Wind Observation around the Tops of the Midlatitude Cirrus by the MU radar and Raman/Mie lidar, *Earth Planets Space*, Vol.61, e33-e36 (Available from <http://www.terrapub.co.jp/journals/EPS/abstract/6107/6107e033.html>).
- Yamamoto, M.K. & Coauthors (2011a). Doppler Velocity Measurement of Portable X-band Weather Radar Equipped with Magnetron Transmitter and IF Digital Receiver, *IEICE Transactions on Communications*, Vol.E94-B, No.6, pp.1716-1724, doi:10.1587/transcom.E94.B.1716.
- Yamamoto, M.K. & Coauthors (2011b). Assessment of Radar Reflectivity and Doppler Velocity Measured by Ka-band FMCW Doppler Weather Radar, *Journal of Atmospheric Electricity*, Vol.31, No.2, pp.85-94.
- Yu, T.-Y., Palmer, R.D. & Hysell, D.L. (2000). A Simulation Study of Coherent Radar Imaging, *Radio Science*, Vol.35, No.5, pp.1129-1141, doi:10.1029/1999RS002236.

- Yu, T.-Y. & Palmer, R.D. (2001). Atmospheric Radar Imaging Using Multiple-Receiver and Multiple-frequency Techniques, *Radio Science*, Vol.36, No.6, pp.1493-1503, doi:10.1029/2000RS002622.
- Yu, T.-Y. & Brown, W.O.J. (2004). High-Resolution Atmospheric Profiling Using Combined Spaced Antenna and Range Imaging Techniques, *Radio Science*, Vol.39, Art.no.RS1011, doi:10.1029/2003RS002907.
- Yu, T.-Y., Furumoto, J.-I. & Yamamoto M. (2010). Clutter Suppression for High-Resolution Atmospheric Observations Using Multiple Receivers and Multiple Frequencies, *Radio Science*, Vol.45, Art.no.RS4011, doi:10.1029/2009RS004330.

IntechOpen



Doppler Radar Observations - Weather Radar, Wind Profiler, Ionospheric Radar, and Other Advanced Applications

Edited by Dr. Joan Bech

ISBN 978-953-51-0496-4

Hard cover, 470 pages

Publisher InTech

Published online 05, April, 2012

Published in print edition April, 2012

Doppler radar systems have been instrumental to improve our understanding and monitoring capabilities of phenomena taking place in the low, middle, and upper atmosphere. Weather radars, wind profilers, and incoherent and coherent scatter radars implementing Doppler techniques are now used routinely both in research and operational applications by scientists and practitioners. This book brings together a collection of eighteen essays by international leading authors devoted to different applications of ground based Doppler radars. Topics covered include, among others, severe weather surveillance, precipitation estimation and nowcasting, wind and turbulence retrievals, ionospheric radar and volcanological applications of Doppler radar. The book is ideally suited for graduate students looking for an introduction to the field or professionals intending to refresh or update their knowledge on Doppler radar applications.

How to reference

In order to correctly reference this scholarly work, feel free to copy and paste the following:

Masayuki K. Yamamoto (2012). New Observations by Wind Profiling Radars, Doppler Radar Observations - Weather Radar, Wind Profiler, Ionospheric Radar, and Other Advanced Applications, Dr. Joan Bech (Ed.), ISBN: 978-953-51-0496-4, InTech, Available from: <http://www.intechopen.com/books/doppler-radar-observations-weather-radar-wind-profiler-ionospheric-radar-and-other-advanced-applications/new-observations-by-wind-profiling-radars>

INTECH
open science | open minds

InTech Europe

University Campus STeP Ri
Slavka Krautzeka 83/A
51000 Rijeka, Croatia
Phone: +385 (51) 770 447
Fax: +385 (51) 686 166
www.intechopen.com

InTech China

Unit 405, Office Block, Hotel Equatorial Shanghai
No.65, Yan An Road (West), Shanghai, 200040, China
中国上海市延安西路65号上海国际贵都大饭店办公楼405单元
Phone: +86-21-62489820
Fax: +86-21-62489821

© 2012 The Author(s). Licensee IntechOpen. This is an open access article distributed under the terms of the [Creative Commons Attribution 3.0 License](#), which permits unrestricted use, distribution, and reproduction in any medium, provided the original work is properly cited.

IntechOpen

IntechOpen